Printing on Fabric Meta-Material for Self-Shaping Architectural Models

David Jourdan[1], Mélina Skouras[2], Etienne Vouga[3], Adrien Bousseau[1]

[1] Université Côte d'Azur, Inria

[2] Université Grenoble Alpes, Inria, CNRS, Grenoble INP, LJK

[3] University of Texas at Austin, Department of Computer Science

Abstract

We describe a new meta-material for fabricating lightweight architectural models, consisting of a tiled plastic star pattern layered over pre-stretched fabric, and an interactive system for computer-aided design of doubly-curved forms using this meta-material. 3D-printing plastic rods over pre-stretched fabric recently gained popularity as a low-cost fabrication technique for complex free-form shapes that automatically lift in space. Our key insight is to focus on rods arranged into repeating star patterns, with the dimensions (and hence physical properties) of the individual pattern elements varying over space. Our star-based meta-material on the one hand allows effective form-finding due to its low-dimensional design space, while on the other is flexible and powerful enough to express large-scale curvature variations. Users of our system design free-form shapes by adjusting the star pattern; our system then automatically simulates the complex physical coupling between the fabric and stars to translate the design edits into shape variations. We experimentally validate our system and demonstrate strong agreement between the simulated results and the final fabricated prototypes.

Keywords: rapid prototyping, architectural modelling, 3D-printing, pre-stretched fabric, form finding, meta-material

1   Introduction

Physical models are an important tool architects use to explore ideas and communicate them to clients and collaborators (Dunn 2014). Architects have a long tradition of exploiting affordable and easy-to-assemble materials for fabricating small-scale prototypes, including cardboard, foam and wood cut-outs. With the rise of maker spaces, technologies for milling, laser cutting, and 3D printing are increasingly accessible and powerful tools for architectural prototyping. Doubly-curved free-form surfaces, however, remain a significant challenge: even with modern additive manufacturing techniques, prototypes of thin curved structures cannot be easily fabricated without form-work, support structures, or other artefacts. In this paper, we introduce a technique for rapid-prototyping lightweight free-form structures, based on 3D-printing a pattern of plastic stars over a pre-stretched piece of fabric. Upon removing the fabric from the 3D printer and allowing it to relax, the fabric and stars exert forces on each other, and the ensemble bends into 3D space to form complex doubly-curved shapes that stand under self-load, as illustrated in fig. 1. We parametrise the star pattern and show that by exploring how the pattern varies spatially over the fabric, a wide variety of surface shapes of various curvatures can be fabricated.

Figure 1: Our printing-on-fabric meta-material encodes surface curvature within a regular star pattern (left). Our predictive simulation allows the virtual design of architectural models (middle), with a close match to physical realization (right).

Our work follows in the line of several recent explorations of combining fabric under tension with 3D-printed networks of elastic rods to control shape (Guberan and Clopath 2016; Agkathidis et al. 2019; Pérez et al. 2017). The resulting fabric and curve structure behaves as a so-called *Kirchhoff-Plateau Surface*, where the fabric forms minimal surface patches bounded by the rods. Yet, a wider variety of shapes are possible if one does not restrict to printing closed curves and instead uses dense repetitive patterns of plastic rods (Kycia 2018; Erioli and Naldoni 2017). Our main contribution is the use of dense 3-pointed star patterns for fabricating free-form structures with large-scale curvature variation. Our choice of 3-pointed stars is based on two important physical observations: first, the arms of the stars bend to

form a small bump localized around the star, which contracts the surface locally. Varying the thickness of the stars offers control on the amount of contraction in their neighbourhood. Second, since the pattern is formed of disconnected elements, the fabric contracts in-between these elements, bringing them closer together, with the amount of contraction controlled by the local spacing of the stars. In both cases, if the amount of contraction varies spatially, it induces in the initially-flat fabric a new rest state with *non-Euclidean metric* (Sharon and Efrati 2010; Kim et al. 2012; Konaković-Luković et al. 2018), and the fabric bends in space to resolve the metric frustration. Due to the combination of these effects, our plastic pattern act as a *meta-material*, whose local geometry dictates the overall shape. Varying the two degrees of freedom offered by the stars thickness and spacing allows us to achieve a variety of shapes, including cylindrical and doubly-curved surfaces with negative gaussian curvature (**fig. 10**). An additional benefit of our star-based approach is that the pattern enriches the surface with a texture, allowing architects to explore a design space that combines shape and appearance.

The precise amount of contraction within and between the stars in a star pattern is determined by the non-linear interaction of the stiff plastic with the fabric substrate. To avoid the need for laborious trial-and-error with physical 3D-printed models, we present a digital tool that simulates how printing-on-fabric meta-materials behave once fabricated, allowing users to quickly iterate on virtual prototypes before investing time in fabrication. To perform our simulation, we introduce a physical model of plastic patterns printed on stretched fabric. Our model goes beyond existing ones (Pérez et al. 2017) by accounting for the bilayer structure of the plastic-on-fabric assemblies and for the specific mechanical behaviour of the structure at the boundary between the patterns and the fabric, especially near the star arms tips, which we found to be critical to accurately reproduce the meta-materials we target. We also detail our fabrication protocol used to achieve accurate, reproducible physical prototypes using a commodity 3D printer.

In summary, we make the following contributions:

- An description of the main physical phenomena that contribute to the emergence of curved surfaces when printing dense plastic patterns over pre-stretched fabric.

- A physical simulator of dense plastic patterns printed on pre-stretched fabric, allowing accurate reproduction of these phenomena.

- A form-finding tool based on this simulator, which we used to design and fabricate a variety of architectural forms based on a simple 3-pointed star pattern.

2   Related work

Our primary goal is to offer computational support for low-cost rapid prototyping of free-form architectural models. The fabrication technique we adopt is low-cost because it only requires commodity fabric and a desktop 3D printer. This technique is also rapid because it only involves printing 2D plastic rods, which automatically stick to the fabric. Once printed and relaxed, the surface deforms on its own to reach an equilibrium, without needing any manual assembly apart from fixing optional boundary positions. We now discuss related work that targets similar goals.

Computational design of deployable surfaces.

Despite the recent development of desktop 3D-printers, printing 3D objects remains a time-consuming and costly procedure because of the large quantity of material that needs to be deposited to support the target 3D surface during its fabrication. This inefficiency of 3D-printing has motivated researchers and practitioners to develop faster alternatives, where a 3D-printer or other fabrication devices are used to produce flat elements that are then deployed to form 3D surfaces. This deployment strategy is also commonly followed in architecture to create large, lightweight structures.

A common challenge faced by this family of methods, including ours, is to modulate the geometry of the flat elements to achieve a target shape. Representative approaches include elastic grid shells that buckle out of plane to follow prescribed boundaries (Du Peloux 2017) or sparse actuation (Panetta et al. 2019), triangular auxetic linkages where the opening angle between adjacent triangles dictates the resulting surface curvature (Konaković-Luković et al. 2018), repetitive spiral-shaped elastic rods where the amount of twist of the spiral controls surface bending (Malomo et al. 2018; Laccone et al. 2019), rigid tiles embedded in a pre-stretched latex membrane where the dihedral angle between adjacent tiles again dictates the resulting curvature (Guseinov et al. 2017), and patterns of low-swelling disks printed within a high swelling substrate where the spatially-varying swelling yields buckling (Kim et al. 2012). Similarly to Kim et al. (2012); Malomo et al. (2018); Konaković-Luković et al. (2018); Guseinov et al. (2017), our approach relies on repetitive parametric elements to encode curvature. However, the relationship between the printed flat layout and the resulting 3D surface is much harder to predict because it involves a complex coupling between elastic plastic rods and elastic fabric. We propose a physical model of printing-on-fabric to simulate this coupling and offer accurate predictions for virtual form-finding.

Printing-on-fabric.

Guberan and Clopath (2016) were among the first to demonstrate the potential of printing-on-fabric to quickly create so-called *self-shaping* prototypes of free-form surfaces. This technique was further explored by Kycia (2018) and Erioli and Naldoni (2017), who experimented with various dense repetitive patterns to achieve different shapes. While these prior attempts inspired our choice of a dense 3-pointed star pattern, they were conducted on a trial-and-error fashion rather than using predictive simulation. Agkathidis et al. (2019) studied the effect of several dense patterns of parallel rods laminated over pre-stretched fabric, and proposed a computational-design workflow to generate a grid of rods aligned with the principal lines of stress of a target shell. While their results show an interesting range of deformations, without using a simulation tool they also had to do multiple physical experiments until reaching a desired shape.

Closer to our approach is the work by Pérez et al. (2017), who simulated printing-on-fabric by modelling the pre-stretched fabric as an elastic membrane, and the printed plastic as elastic rods. However, Pérez et al. (2017) focused on the design of sparse networks of elongated rods, where the stretched fabric forms minimal surfaces bounded by the plastic rods. Their design tool is thus limited to shapes made of panels with vanishing mean curvature. In contrast, we explore the use of a dense repetitive pattern which produces small-scale contractions of the surface, such that mean curvature emerges at large scale. Simulating this pattern required us to adapt the physical model to account for the bilayer nature of the assembly and for the influence of fabric bending on the overall shape.

While the use of a 3D printer to embed plastic into fabric limits the scale of the objects we can produce, Berdos et al. (2020) has shown that similar objects can be created at larger scale by using latex sheets and plywood rods. Kycia (2019) also created large structures by assembling small-scale printed modules. These experiments suggest the potential of printing-on-fabric as a powerful means to create large, lightweight architectural installations.

3   Physical model

To create our star-pattern meta-material, we take a rectangle of thin fabric, pre-stretch it along each dimension by a factor s by pinning the fabric boundary to a wooden frame, place the fabric on the print bed of a 3D-printer, and print small three-pointed stars over the fabric (see **fig. 7**). The melted plastic deposited by the printer adheres to the surface of the fabric, resulting in strong bonding of the two materials to each other. After the plastic has cured, we remove the fabric from the

frame, trim excess fabric, and pose the structure by pinning several points of the boundary to the ground. See **sec. 4** for full details of the fabrication process.

We parameterise the fabric by a rectangle Ω in the plane. Each star's center is placed at the nodes of a regular hexagonal tiling of Ω, with distance d mm between neighbouring centres, with the star's three arms aligned to the symmetry axes of the tiling. Three scalar sizing fields specify the design of the star pattern: $\ell : \Omega \to [0,1]$ specifies the length of the star's arms at different locations on the fabric, with $\ell = 0$ indicating no star at all and $\ell = 1$ a star with arm lengths d (so that the star touches its neighbours); and $h, w : \Omega \to \mathbb{R}$ specify the thickness (in the direction perpendicular to the fabric and printing plane) of the stars and (in-plane) width of the star arms, both in millimetres.

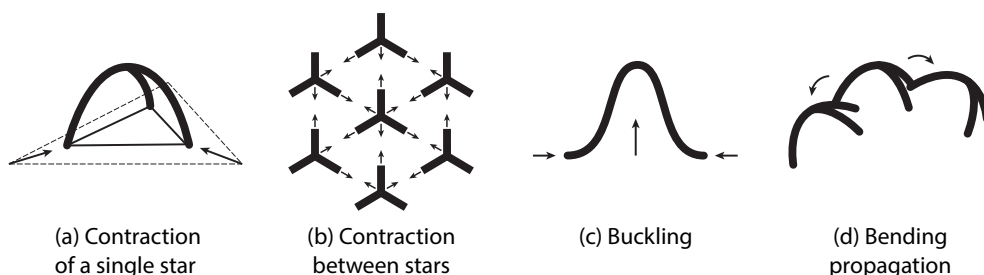To summarize, a star pattern design consists of a choice of:

1. fabric tension s and star spacing d, both global to the entire pattern;

2. three functions ℓ, h, w over Ω; which encode variations in the star sizing;

3. boundary conditions for how the border of the pattern should be pinned to the ground after printing.

3.1 The geometry of the meta-material

After the star pattern has been printed and the fabric is allowed to relax to static equilibrium, the meta-material buckles into a 3D structure with residual internal stress. **Figure 2** illustrates how the choice of design parameters provides several means of lifting the resulting surface into controllable shapes. In the neighbourhood of each individual star, the star arms bend to form a bump under the action of the fabric's compressive forces (**fig. 2a**). The size of this bump depends on the fabric tension s and the length and thickness of the star arms, which control the star's resistance to bending and thus final curvature. In between stars, the fabric contracts unimpeded (**fig. 2b**), by an amount proportional to the length of the star arms.

At a coarse scale much larger than that of an individual star, we can treat the meta-material as a homogenized smooth surface without the bumps around each star. In this homogenized view, the effect of each bump is to change the surface area of a neighbourhood of the star at equilibrium, where the spatially-varying amount of surface contraction depends on the thickness, width, and length of the stars. Therefore ℓ, h, w equip the homogenized surface with a rest state described by a non-Euclidean metric (Sharon and Efrati 2010). In addition to changing the local surface area of the homogenized surface, the stars modify the surface's rest extrinsic

curvature, since the stars are printed on top of the fabric (rather than embedded within it); in other words the metric of the meta-material varies in the thickness as well as the curvilinear directions. The differential contraction described by this metric causes the surface to buckle out of plane, in order to exchange large amounts of stretching strain for slight bending strain (fig. 2c). This relationship between change of metric and buckling has also been exploited by related self-shaping fabrication technologies based on swelling (Kim et al. 2012) or auxetic linkages Konaković-Luković et al. (2018). In our case, the precise relationship between the surface metric and the values of ℓ, h, and w depends on a complex physical coupling between the fabric and the rods.

(a) Contraction of a single star

(b) Contraction between stars

(c) Buckling

(d) Bending propagation

Figure 2: Geometric intuition behind our approach, at several length scales. At the scale of a single star, the contraction of the pre-stretched fabric back to its rest dimensions is arrested by the plastic star bonded to the fabric. The star arms buckle to form a small bump (a); neighbourhoods of thicker stars contract less due to the star arms bending less. At the scale of a neighbourhood of several stars, the fabric contracts unimpeded, since stars are not connected (b). A sparser star pattern with smaller stars (and hence more spacing between them) allows more contraction. At the scale of a large patch of star meta-material, several factors control the surface shape: differential contraction due to variations in star thickness and spacing induces buckling of the surface to relieve metric frustration; boundary conditions can impose additional contraction and buckling (c); and if stars are laid out in a regular pattern, there is global coupling in how each star breaks symmetry while buckling, introducing large-scale curvature (d).

We also observed a coupling phenomenon between neighbouring stars, where the bending of each individual star propagates to adjacent stars through deformation of the fabric in between (fig. 2d). It is unclear whether this behaviour is a consequence of, or an additional effect independent of the induced non-Euclidean metric. This coupling leads to globally consistent symmetry-breaking in the surface, a phenomenon that is especially visible when we do not fix the boundary of the domain, since in this case the accumulation of local bending makes the entire surface fold on itself to form a tube, as shown in fig. 3.

Given the complexity of the physical phenomena involved, from local contraction of the surface to global propagation of bending, we propose a dedicated numerical simulation to predict the shape that user-provided star patterns would take.
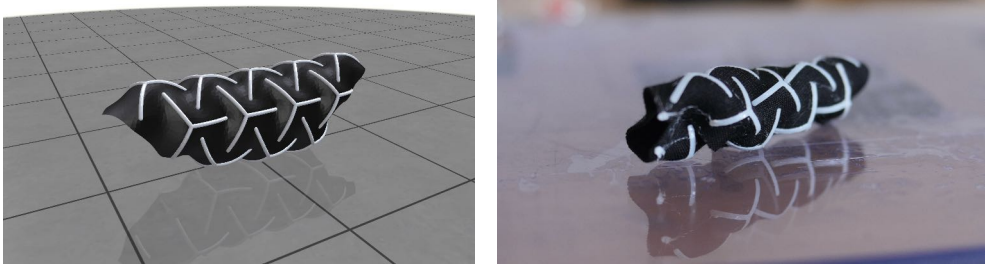
Figure 3: Our simulation tool (left) correctly predicts that a uniform star pattern, with free boundary, rolls up into a cylinder at static equilibrium (right). This complex behaviour is due to the extrinsic curvature induced by the bilayer structure of the rod-and-fabric assembly, and the coupling of the bending of neighbouring stars causing global symmetry-breaking in the pattern.

3.2 Numerical simulation

We model the fabric as a plate discretised using constant strain triangles and edge-based bending hinges (Grinspun et al. 2003) and we use discrete elastic rods (Bergou et al. 2010) for modelling the arms of the stars. We enforce the coupling between the plate and the rods via collocation: all centreline degrees of freedom of the rod are also vertices of the plate. This strategy implies that the fabric mesh must have edges that align with the star arms: we first discretise the rods constituting each star (by choosing the resolution of the rod centreline) and then we generate the fabric mesh using constrained Delaunay triangulation (Shewchuk 1996). Compared to the model of Pérez et al. (2017), our implementation additionally relies on three distinguishing features that we found to be critical for successfully simulating the behaviour of the structures: a rest curvature for the rods accounting for the bilayer structure of the star meta-material, a non-linear material model for the fabric, and an energy term capturing the coupling of the three rods meeting at each star centre.

Bilayer rod model.

Simply collocating the rods representing star arms to the thin shell model representing the fabric does not correctly capture the geometry of the rod-on-fabric assembly: in the printed assembly, the stars are *on top* of the fabric, while in the collocation model, rods are embedded *within* the fabric. Yet the bilayer structure of the assembly is precisely what causes the rods to bend in a privileged direction, due to the differences in stresses between the traction-free top surface of the rod and the compressive forces applied by the fabric to the bottom surface. We can easily observe this so-called *bilayer effect* on a flat rod printed on top of a strip of fabric of the same width: the structure will not stay flat when released and will consistently bend in the same direction (see **fig. 4**, left).
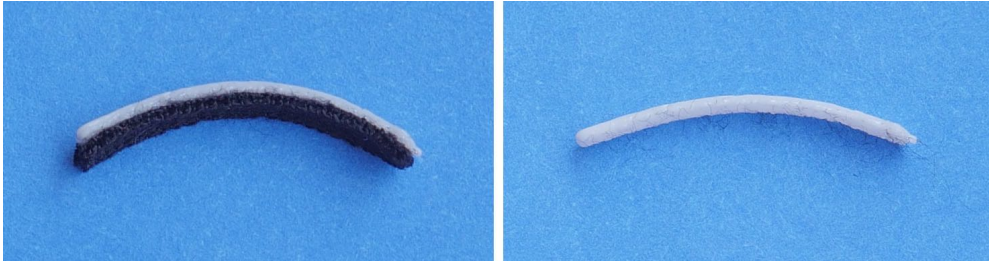
Figure 4: A plastic rod printed on top of a strip of fabric. Due to the bilayer effect, the rod will naturally bend upwards (left). The plasticity of the material causes the upper layer not to recover its initially flat shape when detached from the fabric layer (right).

Furthermore, the assembly also exhibits some plastic deformation: when we separate the rod from the fabric layer, the initially straight rod does not completely recover its original shape (see **fig. 4**, right) and has a non-zero rest curvature $\bar{\kappa}$. As noted by van Rees et al. (2017), we can derive general shell equations for bilayers based on their respective thicknesses and their Young's moduli. We adapted their formulas to the case of our non-planar strips, and, as detailed in the appendix, we show that the bilayer is energetically equivalent to a mono-layer with rest curvature κ given by

$$\kappa = \frac{6h_2(h_1 + h_2)}{h_1^3}\frac{E_2}{E_1}(1 - \frac{1}{s^2}) + \bar{\kappa}, \tag{1}$$

where $h_1 = h(x,y)$ is the thickness of the star arm, h_2 the (constant) thickness of the fabric, and E_1 and E_2 the Young's moduli of the rod and fabric, respectively. We use this expression to set the rest curvature of the rods about their width axis. This model allows us to accurately reproduce the global curling up of a uniform star pattern into a rolled tube; see **fig. 3**. We provide in **fig. 5** a comparison between our model and a model that ignores this bilayer effect, showing that our model better captures the behaviour of a real-world fabricated surface.

Fabric's material model.

Our structures exhibit high localized stresses and large deformations near the tips of the stars arms, due to the arm tips bending and "digging into" the fabric substrate. Using a linear material model for the fabric causes elements to completely compress and eventually invert in these regions; instead we use a Neo-Hookean material model to approximate the non-linear deformation of the fabric near the rod tips. Furthermore, while bending forces are typically much smaller than membrane forces in Kirchhoff-Plateau surfaces and can be mostly neglected (Pérez et al. 2017), we found that accounting for the finite flexural resistance of the material at the boundary between the stars and fabric was necessary to limit the tangent discontinuities at the boundary and to reproduce the global curvature of the surface

that we observed on the real artefacts (see **fig. 5**). We followed the implementation of the Discrete Shells energy suggested by Tamstorf and Grinspun (2013) and defined the bending coefficient of the flexural term as $k_B = \frac{Eh^3}{24(1-\nu^2)}$, where h is the thickness of the membrane, E its Young's modulus and ν its Poisson's ratio. Note that despite the small orthotropy exhibited by the fabric that we used, modelling it as an isotropic material was enough to capture the global behaviour of the structure.

| (a) No bending | (b) No bilayer | (c) Our model | (d) Fabrication |
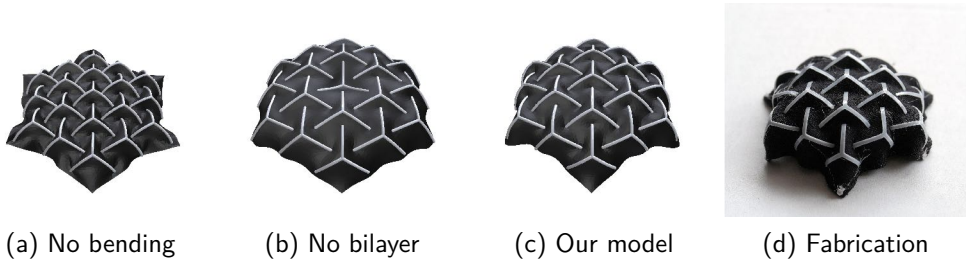
Figure 5: Impact of critical components of our model when simulating a uniform field of stars. **(a)** Neglecting bending forces in the fabric makes the stars contract independently of each other, preventing the emergence of global curvature. **(b)** Using a flat rest shape for the rods makes the stars less curved than in reality. **(c,d)** Our complete model better reproduces the built surface.

Rod connections.

We compute rod stretching, bending, and twisting energies and forces as described by Bergou et al. (2008, 2010). One complication is that the model of Bergou et al. does not discuss connections between rods. While defining energies that allow for proper transfer of bending and twisting forces from one rod to the other is, in the general case, a challenging problem (Pérez et al. 2015), the three-fold symmetry of our stars allows for a simple treatment : we compute twist and bending at the connection as if each star arm were split into two "copies" of the same rod with the same geometry and each was bonded to one rod copy on each of the two other arms (see inset figure). The elastic energy contributed by the connection is then the sum of the three pairwise bending and twisting energies, weighted by $\frac{1}{2}$ since the cross-sectional area of each "rod copy" is half that of the full rod.
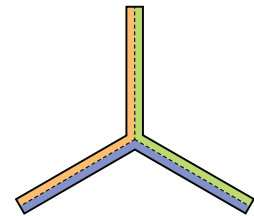
Figure 6: To define a bending and twisting energy at the connection between three rods, we split each rod into two copies, and divide the volume of the connection into three equal parts consisting of pairwise rod connections, here shown in different colours.

Optimization.

Starting from a flat initial guess, we compute the equilibrium shape of a star pattern by minimizing the total energy of the system using a Newton-Raphson procedure with line search. We regularize Hessian (by adding a multiple of the identity matrix)

whenever the Hessian fails to be positive definite (Nocedal and Wright 2006). We report the runtime performances of this minimization procedure for all the examples shown in the paper in **tab. 1**.

4   Fabrication

We now describe the hardware setup we used to produce our physical models, shown in **fig. 7**. Our substrate is an elastic polyurethane fabric. We used a stretch factor of $s = 1.35$ (in both directions) in all of our experiments. To hold the fabric in place under tension, we built a custom, 26 by 26cm wooden frame and clamp the fabric between the frame and a plexiglass plate of similar dimensions (see **fig. 7**), which we fix to the print bed with magnets. To confirm that the fabric has been installed in its frame at the proper tension, we use a fabric marking pencil to draw a square with side length 10 cm near the centre of the fabric before stretching it, and check that the square has side length $10s$ cm once the fabric is clamped in its frame.
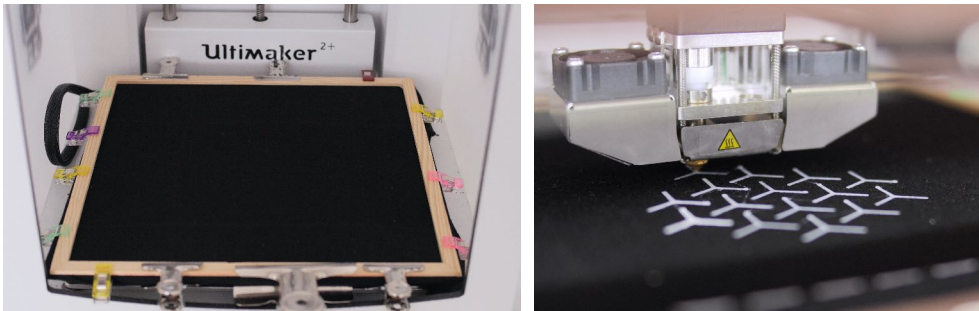
Figure 7: Our 3D printing setup. We stretch the fabric and clamp it between a wooden frame and a plexiglass plate, which we attach to the build plate with magnets (left). The printer deposits plastic on the surface of the stretched fabric (right).

In contrast to prior work (Pérez et al. 2017) that used standard PLA printing filament, we performed our experiments using a more flexible TPU95A plastic to allow finer-grained control and higher range of star bending stiffness. We employ a UltiMaker2+ printer, which performs well with flexible filament. The printer must be calibrated to account for the thickness of the fabric and plate effectively raising the height of the print bed; we observed that without proper calibration to ensure that nozzle begins directly above the fabric when extruding the first star layer, the melted plastic does not stick well to the fabric.

The material properties of printing filament can vary widely even between different spools of the same material purchased from the same manufacturer. To avoid relying on inaccurate material parameters from a material datasheet, we used **eq. (1)** to directly calibrate the relative Young's modulus of the plastic with

respect to the fabric. We printed 4×10 strips of plastic of known thicknesses h_1 ranging from 0.3 mm to 0.45 mm over the fabric, and trimmed the fabric around each strip to produce a beam whose cross-section is a fabric-plastic bilayer. This beam flexes out of plane into a circular arc of approximately constant curvature; we photograph the side view (see **fig. 4**, left) and estimated the beam's natural curvature κ from the dimensions of the bounding rectangle in the image plane. We then carefully removed the bottom fabric layer from the plastic rod and measured its rest curvature $\bar{\kappa}$ the same way (see **fig. 4**, right). Since we know the fabric's thickness $h_2 = 0.8$ mm from measurements, the stretch factor $s = 1.35$, and the thickness h_1 of each printed plastic strip, we use linear regression and **eq. (1)** to deduce the ratio of Young's moduli $E_1/E_2 = 3.2 \times 10^3$.

5 Evaluation

We first present several simulation experiments that illustrate how our model behaves with typical parameter settings. We then demonstrate the potential of our approach for architectural modelling by designing and fabricating a variety of free-form surfaces.

Effect of parameters.

As described in **sec. 3**, the amount of contraction of the surface is influenced both by the arm length ℓ and thickness h of the stars. **Figure 8** illustrates the effect of these two parameters when we vary them according to a linear radial gradient over a hexagonal domain. Setting ℓ smaller at the boundary of the domain and larger in the centre gives more room for contraction at the boundary than in the middle, inducing the surface to buckle into a dome-like shape. A similar effect is achieved by using thinner stars on the boundary. In contrast, using long or thick stars at the boundary prevents contraction, so that the surface shape near the centre is flatter. Using thick stars also results in smoother surfaces overall, while thin stars decorate the surface with multiple small bumps. While both thickness and arm length can be varied at the same time, we observed that ℓ usually has a greater effect on curvature, and so we used a fixed thickness of $h = 0.3$ mm for all other results. We also experimented with variations in arm width w, but this parameter had less impact that h on the surface shape — consistent with the fact that the bending stiffness of the star arms scales cubically in the arm thickness, but only linearly in its width.

Equipped with the ability to vary surface contraction locally, we can achieve different amounts of curvature by adjusting the rate of change of surface contraction. **Figure 9** illustrates this control on a hexagonal domain fixed at its boundary, where

we vary the size of the stars according to radial gradients of different profiles to produce surfaces ranging from a bell shape to a cone. For illustration purposes, we use a stronger stretching factor $s = 1.75$ in this experiment.


Figure 8: We show the effect of two design parameters on the equilibrium shape of the star meta-material: the length of the star arms ℓ and their thickness h. For this experiment we print 37 stars on a hexagon of fabric with side length 67 mm. In the top row we fixed $\ell = 10$ mm and set, from left to right, h with a decreasing radial gradient from 0.6 mm to 0.2 mm, a constant value of 0.4 mm and an increasing gradient from 0.2 to 0.6 mm. In the bottom row we fix $h = 0.3$ mm and prescribe three different radial gradients for ℓ: a decreasing gradient from 10 mm to 4 mm, and constant value of 7 mm and an increasing gradient from 4 mm to 10 mm.
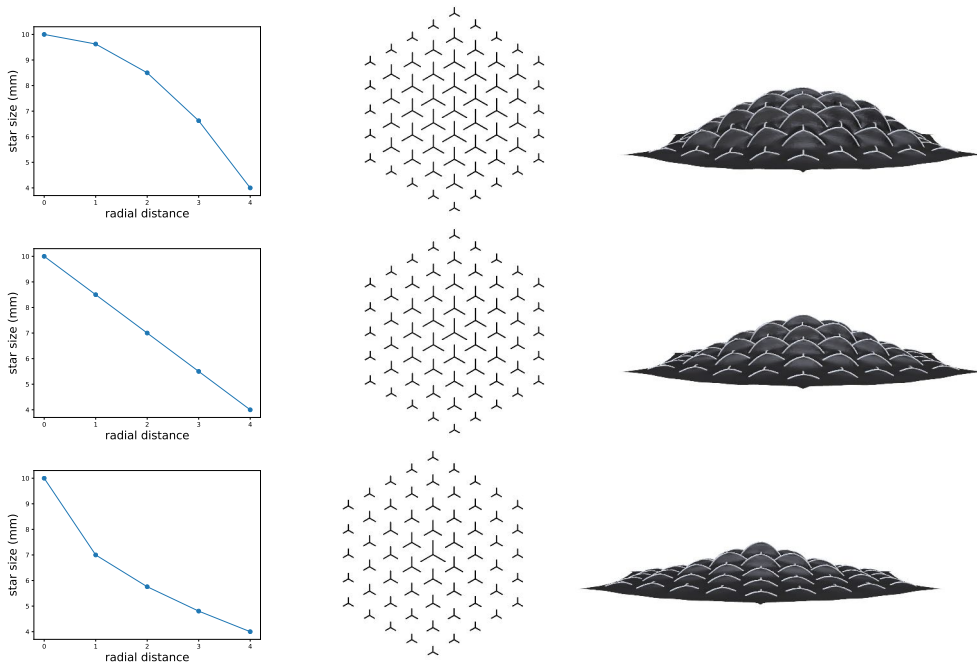
Figure 9: Effect of different arm-length gradient profiles on the equilibrium shape of a hexagonal star pattern. Each row corresponds to a different function $\ell(x, y)$: on the left, a plot of ℓ as a function of distance to the hexagon center; in the middle, a diagram of the corresponding star pattern design; and on the right, the simulated equilibrium shape.

Example designs.

Figures 1 and **10** showcase several architectural models that we created with our approach. For each result, we provide the input star pattern, the simulated surface, and a picture of the fabricated model. In all cases, we observe a close agreement between our simulation and reality.

| Star pattern | Simulation | Fabrication |
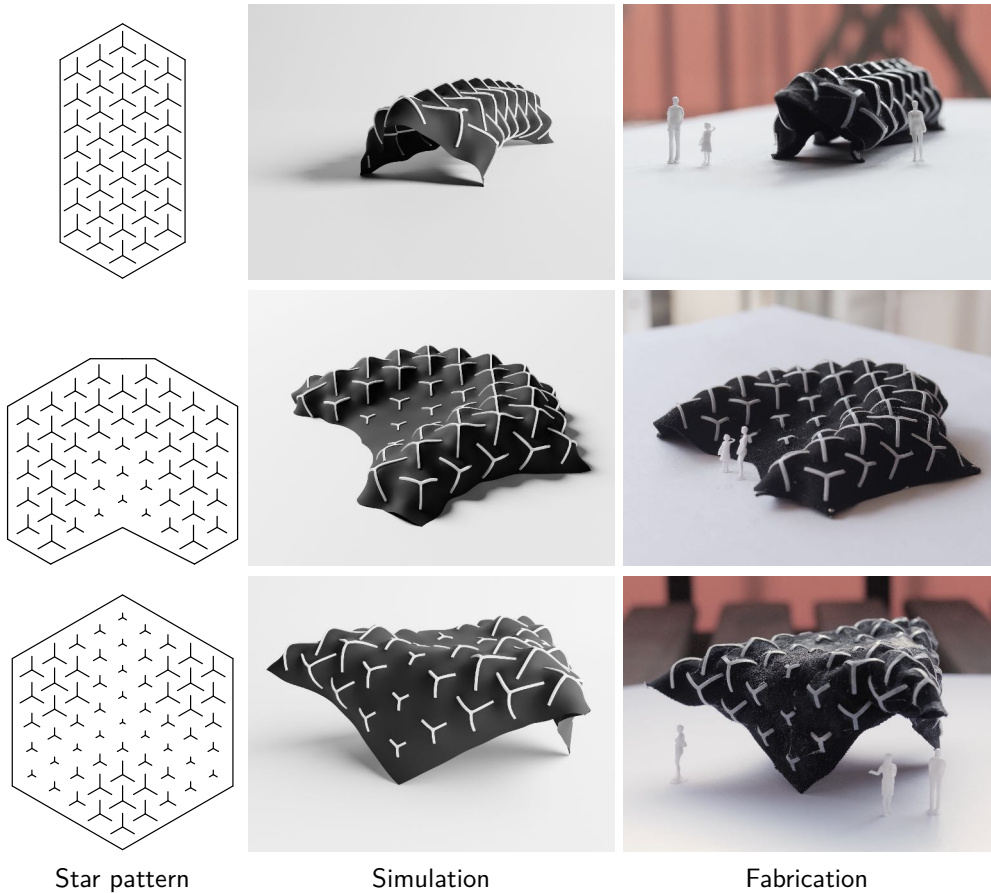
Figure 10: Various architectural models created using our system, from top to bottom: a U-shape, a tunnel and a doubly-curved roof. For each result we provide the star layout to be printed (left), the simulated surface (middle), and the printed result (right).

Figure 1 shows a cylindrical section with varying star sizes supported by six needles to model a small roof. The first row of **fig. 10** shows a more curved cylindrical tunnel composed of a uniform field of stars, which we fixed to the ground along two of its edges to prevent it to fold on itself. The second row shows the result of a layout where large stars form a U-shaped boundary, while smaller stars contract the surface in its centre. The resulting surface takes the shape of an amphitheatre. Only points along the U-shaped boundary were fixed. The third row is a doubly-

curved surface that we obtained using a hexagonal domain where we made the stars smaller in the middle and towards its three fixed corners. The three other corners are covered by bigger stars, which prevent them to contract as much as their surroundings, yielding buckling. We also applied a textile hardener (Powertex) so that this surface supports its own weight.

Printing our models took 20 minutes on average, we refer to **tab. 1** for simulation runtimes.

Name	Runtime	Nb of vertices
roof (**fig. 1**)	17m27,713s	7237
U shape	28m22,730s	10551
tunnel	23m57,832s	8020
doubly-curved	40m0,354s	12140

Table 1: Runtime performance of the simulation on a PC with an Intel Xeon Gold 5118 processor running at 2.60GHz (single-threaded).

6 Conclusion and future work

We presented a new meta-material made of plastic star patterns printed over pre-stretched fabric and showed that by changing the thicknesses of the stars and their density we could modulate the shapes of the resulting 3D structures.

While the simulator that we proposed proved to be effective for exploring the design space spanned by this material, finding the exact star parameters corresponding to a specific target shape remains a difficult task. One possible approach to reach this goal could be to integrate our forward simulation method into an inverse design procedure based, *e.g.*, on constrained optimization. By flattening the desired target shape using conformal mapping and by mapping the star parameters to metric distortion, initial values for the star sizes could be obtained and used as initial guess for this non-linear optimization. An interesting avenue for future work would be to leverage the regularity of our patterns to derive an *homogenised* material model capturing the macro-scale behaviour of our structures by abstracting away fine-scale phenomena. Such a model would be useful to speed-up computations. In addition, while we focused on simple 3-pointed stars, our simulator could generalize to a wide variety of patterns to offer practitioners with a palette of meta-materials with varied appearance and physical properties.

Our results demonstrate that a regular pattern of elastic rods can yield the emergence of global mean curvature from what behaves locally as a minimal surface. While the actuation mode that we exploit, stretching, limits our technique to the design

of models for now, we hope that this work will inspire the design of large-scale lightweight architectural structures with rich curvature.

Acknowledgements

References

Agkathidis, A., Y. Berdos, and A. Brown (2019). Active membranes: 3d printing of elastic fibre patterns on pre-stretched textiles. *International Journal of Architectural Computing 17*(1), 74–87.

Berdos, Y., A. Agkathidis, and A. Brown (2020). Architectural hybrid material composites: computationally enabled techniques to control form generation. *Architectural Science Review 63*(2), 154–164.

Bergou, M., B. Audoly, E. Vouga, M. Wardetzky, and E. Grinspun (2010, July). Discrete viscous threads. *ACM Trans. Graph. 29*(4), 116:1–116:10.

Bergou, M., M. Wardetzky, S. Robinson, B. Audoly, and E. Grinspun (2008, aug). Discrete Elastic Rods. *ACM Transactions on Graphics (SIGGRAPH) 27*(3), 63:1–63:12.

Du Peloux, L. (2017). *Modeling of bending-torsion couplings in active-bending structures : application to the design of elastic gridshells*. Ph. D. thesis.

Dunn, N. (2014). *Architectural Modelmaking*. Laurence King Publishing.

Erioli, A. and L. Naldoni (2017). informed flexible matter workshop. `http://www.co-de-it.com/wordpress/informed-flexible-matter.html`.

Grinspun, E., A. N. Hirani, M. Desbrun, and P. Schröder (2003). Discrete shells. In *Proceedings of the 2003 ACM SIGGRAPH/Eurographics Symposium on Computer Animation*, SCA '03, Aire-la-Ville, Switzerland, Switzerland, pp. 62–67. Eurographics Association.

Guberan, C. and C. Clopath (2016). Active shoes. `https://selfassemblylab.mit.edu/active-shoes`. MIT Self-Assembly Lab.

Guseinov, R., E. Miguel, and B. Bickel (2017). Curveups: Shaping objects from flat plates with tension-actuated curvature. *ACM Transactions on Graphics (Proc. SIGGRAPH) 36*(4).

Kim, J., J. A. Hanna, M. Byun, C. D. Santangelo, and R. C. Hayward (2012). Designing responsive buckled surfaces by halftone gel lithography. *Science 335*(6073), 1201–1205.

Konaković-Luković, M., P. Konaković, and M. Pauly (2018). Computational design of deployable auxetic shells. In *Advances in Architectural Geometry 2018*.

Konaković-Luković, M., J. Panetta, K. Crane, and M. Pauly (2018). Rapid deployment of curved surfaces via programmable auxetics. *ACM Transactions on Graphics (Proc. SIGGRAPH) 37*(4).

Kycia, A. (2018). Material form-finding of modular textile structures. In *CA^{2}RE: Conference for Artistic and Architectural (Doctoral) Research*, Denmark, pp. 331–341. Arkitektskolen Aarhus.

Kycia, A. (2019). Hybrid textile structures as means of material-informed design strategy. In M. Ballestrem, I. Borrego, D. Fioretti, R. Pasel, and J. Weidinger (Eds.), *CA^{2}RE Berlin Proceedings: Conference for Artistic and Architectural (Doctoral) Research*, Berlin, pp. 34–35. Universitätsverlag der TU Berlin.

Laccone, F., L. Malomo, J. Pérez, N. Pietroni, F. Ponchio, B. Bickel, and P. Cignoni (2019, oct). Flexmaps pavilion: a twisted arc made of mesostructured flat flexible panels. In *FORM and FORCE, IASS Symposium 2019, Structural Membranes 2019*, pp. 498–504.

Malomo, L., J. Pérez, E. Iarussi, N. Pietroni, E. Miguel, P. Cignoni, and B. Bickel (2018). Flexmaps: Computational design of flat flexible shells for shaping 3d objects. *ACM Transactions on Graphics (Proc. SIGGRAPH Asia) 37*(6), 14.

Nocedal, J. and S. Wright (2006). *Numerical Optimization*. Springer.

Panetta, J., M. Konaković-Luković, F. Isvoranu, E. Bouleau, and M. Pauly (2019). X-shells: A new class of deployable beam structures. *ACM Transactions on Graphics (Proc. SIGGRAPH) 38*(4).

Pérez, J., M. A. Otaduy, and B. Thomaszewski (2017, July). Computational design and automated fabrication of kirchhoff-plateau surfaces. *ACM Trans. Graph. 36*(4), 62:1–62:12.

Pérez, J., B. Thomaszewski, S. Coros, B. Bickel, J. A. Canabal, R. Sumner, and

M. A. Otaduy (2015, July). Design and fabrication of flexible rod meshes. *ACM Trans. Graph. 34*(4), 138:1–138:12.

Sharon, E. and E. Efrati (2010). The mechanics of non-euclidean plates. *Soft Matter 6*, 5693–5704.

Sharp, N. et al. (2019). Polyscope. www.polyscope.run.

Shewchuk, J. R. (1996). Triangle: Engineering a 2d quality mesh generator and delaunay triangulator. In *Selected Papers from the Workshop on Applied Computational Geormetry, Towards Geometric Engineering*, FCRC '96/WACG '96, London, UK, UK, pp. 203–222. Springer-Verlag.

Tamstorf, R. and E. Grinspun (2013, November). Discrete bending forces and their jacobians. *Graph. Models 75*(6), 362–370.

van Rees, W. M., E. Vouga, and L. Mahadevan (2017). Growth patterns for shape-shifting elastic bilayers. *Proceedings of the National Academy of Sciences 114*(44), 11597–11602.

Appendix: Derivation of the rest curvature of a mono-layer rod corresponding to a rod-on-fabric bilayer

In this appendix, we detail the derivation of the rest curvature of a mono-layer rod energetically equivalent to a rod-on-fabric bilayer (eq. (1)).

van Rees et al. (2017) show that a bilayer shell made of two monolayers of respective Young's moduli E_1, E_2 and thicknesses h_1, h_2, and where the strain-free rest state of each layer is given by a different metric (i.e. first fundamental form) $\mathbf{a}_{r_1}$ and $\mathbf{a}_{r_2}$, is energetically equivalent to a mono-layer with non-zero rest curvature. They give formulas for the rest first and second fundamental forms $\mathbf{a}_r$ and $\mathbf{b}_r$ of this equivalent mono-layer (see 1.3.3 in their supplemental material). To account for rod plasticity, we extend their formula to the case where each of the two layers in the bilayer have non-flat rest shape with same second fundamental form $\bar{\mathbf{b}}$.[1] Here we derive new formulas for $\mathbf{a}_r$ and $\mathbf{b}_r$ that account for this bilayer rest curvature.

To this end, we make the following ansatz:

$$\mathbf{a}_{r_1} = \mathbf{a}_r + \alpha_1(\mathbf{b}_r - \bar{\mathbf{b}})$$
$$\mathbf{a}_{r_2} = \mathbf{a}_r - \alpha_2(\mathbf{b}_r - \bar{\mathbf{b}}),$$
(2)

---

[1]Note that in our case, only the plastic rod exhibits significant plasticity. However, assuming that the fabric has the same curved rest state as the rod helps simplifying the formulas. Since our fabric is highly flexible, we believe that the error that we introduce by doing so is negligible.

where α_1 and α_2 are factors to be determined so that the elastic energy of the effective mono-layer and that of the bilayer agree up to a constant. Note that for any choice of these factors, eq. (2) is satisfied by setting

$$\mathbf{a}_r = \frac{\mathbf{a}_{r_1} + \mathbf{a}_{r_2}}{2} - \frac{\alpha_1 - \alpha_2}{2(\alpha_1 + \alpha_2)}(\mathbf{a}_{r_1} - \mathbf{a}_{r_2}) \tag{3}$$

$$\mathbf{b}_r = \bar{\mathbf{b}} + \frac{\mathbf{a}_{r_1} - \mathbf{a}_{r_2}}{\alpha_1 + \alpha_2}. \tag{4}$$

Like van Rees et al. (2017), we define the elastic inner product associated to a material with Poisson's ratio ν as

$$< \mathbf{A}, \mathbf{B} >= \frac{\nu}{1 - \nu^2}\mathrm{Tr}(\mathbf{A})\mathrm{Tr}(\mathbf{B}) + \frac{1}{1 + \nu}\mathrm{Tr}(\mathbf{AB}) \tag{5}$$

and the elastic energy norm as

$$||\mathbf{A}||^2 =< \mathbf{A}, \mathbf{A} >= \frac{\nu}{1 - \nu^2}\mathrm{Tr}^2(\mathbf{A}) + \frac{1}{1 + \nu}\mathrm{Tr}(\mathbf{A}^2). \tag{6}$$

Letting $\mathbf{a}_c$ and $\mathbf{b}_c$ denote, respectively, the first and second fundamental forms of the mid-surface of the shell in the current configuration, we can define the energy of the bilayer by

$$
\begin{aligned}
E_{BL} = \frac{1}{2}\int_U E_1 &\left[\frac{h_1}{8}||\mathbf{a}_{r_1}^{-1}\mathbf{a}_c - \mathbf{I}||^2 + \frac{h_1^3}{24}||\mathbf{a}_{r_1}^{-1}(\mathbf{b}_c - \bar{\mathbf{b}})||^2 \right. \\
&\left. + \frac{h_1^2}{8} < \mathbf{a}_{r_1}^{-1}\mathbf{a}_c - \mathbf{I}, \mathbf{a}_{r_1}^{-1}(\mathbf{b}_c - \bar{\mathbf{b}}) > \right]\sqrt{\det\mathbf{a}_{r_1}}\,\mathrm{d}x\mathrm{d}y \\
+ \frac{1}{2}\int_U E_2 &\left[\frac{h_2}{8}||\mathbf{a}_{r_2}^{-1}\mathbf{a}_c - \mathbf{I}||^2 + \frac{h_2^3}{24}||\mathbf{a}_{r_2}^{-1}(\mathbf{b}_c - \bar{\mathbf{b}})||^2 \right. \\
&\left. - \frac{h_2^2}{8} < \mathbf{a}_{r_2}^{-1}\mathbf{a}_c - \mathbf{I}, \mathbf{a}_{r_2}^{-1}(\mathbf{b}_c - \bar{\mathbf{b}}) > \right]\sqrt{\det\mathbf{a}_{r_2}}\,\mathrm{d}x\mathrm{d}y
\end{aligned}
\tag{7}
$$

and that of the equivalent mono-layer by

$$
\begin{aligned}
E_{ML} = \frac{1}{2}\int_U &\left[\frac{E_1 h_1 + E_2 h_2}{8}||\mathbf{a}_r^{-1}\mathbf{a}_c - \mathbf{I}||^2 + \frac{E_1 h_1^3 + E_2 h_2^3}{24}||\mathbf{a}_r^{-1}(\mathbf{b}_c - \mathbf{b}_r)||^2 \right. \\
&\left. + \frac{E_1 h_1^2 - E_2 h_2^2}{8} < \mathbf{a}_r^{-1}\mathbf{a}_c - \mathbf{I}, \mathbf{a}_r^{-1}(\mathbf{b}_c - \mathbf{b}_r) > \right]\sqrt{\det\mathbf{a}_r}\,\mathrm{d}x\mathrm{d}y,
\end{aligned}
\tag{8}
$$

where U is the parameterisation domain of the shell mid-surface parameterised by curvilinear coordinates (x, y).

After plugging **eq. (2)** in **eq. (7)**, expanding the terms inside the norms, discarding all terms which do not depend on $\mathbf{a}_c$ nor $\mathbf{b}_c$ (and therefore do not change the equilibrium state), and equating all the remaining terms, we find that E_{BL} matches E_{ML} (up to a constant) when the following system of equations is satisfied:

$$
\begin{aligned}
\frac{E_2 h_2 \alpha_2 - E_1 h_1 \alpha_1}{4} &= \frac{1}{8}(E_2 h_2^2 - E_1 h_1^2) \\
\frac{E_1 h_1^2 \alpha_1 + E_2 h_2^2 \alpha_2}{8} &= \frac{1}{12}(E_2 h_2^3 + E_1 h_1^3).
\end{aligned}
\tag{9}
$$

Solving System **eq. (9)** for α_1 and α_2 gives us

$$
\begin{aligned}
\alpha_1 &= \frac{4h_1^3 E_1 + 3h_1^2 h_2 E_1 + h_2^3 E_2}{6h_1^2 E_1 + 6h_1 h_2 E_1} \\
\alpha_2 &= \frac{h_1^3 E_1 + 3h_1 h_2^2 E_2 + 4h_2^3 E_2}{6h_1 h_2 E_2 + 6h_2^2 E_2},
\end{aligned}
\tag{10}
$$

which allows us to write

$$
\mathbf{b}_r - \bar{\mathbf{b}} = \frac{\mathbf{a}_{r_1} - \mathbf{a}_{r_2}}{\alpha_1 + \alpha_2} = \frac{6h_1 h_2 E_1 E_2 (h_1 + h_2)}{h_1^4 E_1^2 + 2h_1 h_2 E_1 E_2 (2h_1^2 + 3h_1 h_2 + 2h_2^2) + h_2^4 E_2^2}(\mathbf{a}_{r_1} - \mathbf{a}_{r_2}).
\tag{11}
$$

The plastic material that we use is much stiffer than the fabric, i.e. $E_1 >> E_2$, so we can further simplify this expression:

$$
\mathbf{b}_r - \bar{\mathbf{b}} \approx \frac{6h_2 (h_1 + h_2) E_2}{h_1^3 E_1}(\mathbf{a}_{r_1} - \mathbf{a}_{r_2}).
\tag{12}
$$

We assume the plastic printed on top of the stretched fabric has no residual strain, so that the metric of the plastic is $\mathbf{a}_{r_1} = \begin{pmatrix} 1 & 0 \\ 0 & 1 \end{pmatrix}$. Since the fabric is stretched from rest by a factor s, $\mathbf{a}_{r_2} = \begin{pmatrix} \frac{1}{s^2} & 0 \\ 0 & \frac{1}{s^2} \end{pmatrix}$. We then have

$$
\mathbf{b}_r - \bar{\mathbf{b}} \approx \frac{6h_2 (h_1 + h_2) E_2}{h_1^3 E_1} \begin{pmatrix} 1 - \frac{1}{s^2} & 0 \\ 0 & 1 - \frac{1}{s^2} \end{pmatrix},
\tag{13}
$$

i.e.,

$$
\mathbf{b}_r \approx \frac{6h_2 (h_1 + h_2) E_2}{h_1^3 E_1} \begin{pmatrix} 1 - \frac{1}{s^2} & 0 \\ 0 & 1 - \frac{1}{s^2} \end{pmatrix} + \bar{\mathbf{b}}.
\tag{14}
$$

The bending energy of the rod-on-fabric assembly will penalize deviation of the assembly's second fundamental form $\mathbf{b}_c$ away from $\mathbf{b}_r$. Since the arms of our stars are much longer than they are wide, we neglect bending deformations in the width direction, and assume that the arms are at rest when the curvature κ in the longitudinal direction matches the normal curvature in that direction prescribed by $\mathbf{b}_r$:

$$\kappa = \frac{6h_2(h_1 + h_2)E_2}{h_1^3 E_1}\left(1 - \frac{1}{s^2}\right) + \bar{\kappa}, \tag{15}$$

where $\bar{\kappa}$ is the rest curvature of the plastically deformed rod in the longitudinal direction.